Article

Variable-Angle Random High-Frequency Voltage Injection Strategy with Cross-Saturation Effect Compensation for Sensorless Synchronous Reluctance Motor Drives

Liangnian Lv [1], Ziming Hu [2], Sisi Li [2], Rui Guo [1], Jinpeng Wang [1,*], Gaolin Wang [2] and Shulin Li [1]

[1] Goldwind Science & Technology Co., Ltd., No. 8 Boxing 1st Road, Economic & Technological Development District, Beijing 100176, China; lvliangnian@goldwind.com (L.L.); guorui1@goldwind.com (R.G.); lishulin@goldwind.com (S.L.)
[2] School of Electrical Engineering and Automation, Harbin Institute of Technology, Harbin 150001, China; huzm25@midea.com.cn (Z.H.); 1180610712@stu.hit.edu.cn (S.L.); wgl818@hit.edu.cn (G.W.)
[*] Correspondence: wangjinpeng@goldwind.com

Abstract: There are usually noise problems when the position sensorless control of a synchronous reluctance motor (SynRM) is carried out by high-frequency (HF) signal injection method. Due to the special structure, the cross-saturation effect of the SynRM is particularly serious, resulting in reduced position observation accuracy. In this paper, a variable-angle random HF voltage injection strategy with cross-saturation effect compensation is proposed for position sensorless SynRM drives. Random number generation based on the chaotic mapping method is used to generate random HF voltage signals with different frequencies for injection; the current power spectral density (PSD) distribution is extended and the HF noise can be reduced. A control strategy based on variable-angle square-wave injection is proposed to suppress the cross-saturation effect. By measuring the position error curves of different loads off-line and polynomial fitting the curves, the position error is achieved by combining with the corresponding signal demodulation algorithm. The proposed method does not require additional hardware resources and can maintain high control accuracy and robustness. Finally, the effectiveness of the proposed sensorless control strategy is verified on a 3 kW SynRM experimental platform.

Keywords: synchronous reluctance motor; random HF voltage injection; variable-angle square-wave injection; cross-saturation effect compensation

1. Introduction

The synchronous reluctance motor (SynRM), which has been widely used in industrial applications, has the advantages of high efficiency, simple structure, no need for a permanent magnet and so on [1,2]. The rotor position detection is of great importance for vector control because it directly affects motor performance and efficiency. Position sensors such as encoders are usually used to obtain position information. However, the installation of such sensors can significantly increase the cost, reduce the reliability and hinder the application in the industrial fields [3]. There are also some disadvantages such as difficult installation and high cost [3–8]. Sensorless control technology has become a research focus in recent years because it reduces drive costs and mechanical complexity while increasing system reliability and operating environment adaptability.

According to the different speed ranges, sensorless control can be divided into two categories. At medium and high speed, the rotor position is usually observed by the method based on the back electromotive force or flux linkage model. However, at zero and low speed, the estimation accuracy decreases with the speed due to the reduction in the signal-to-noise ratio, which usually needs to inject additional signals at zero and low speed to improve it. In addition, because of the special rotor structure of the SynRM,

the signal injection scheme based on the salient pole characteristics of the rotor makes it easier to realize sensorless control. Therefore, the high-frequency (HF) signal injection method has been widely studied [9–15]. The HF injection method is usually divided into the HF sinusoidal injection method and the HF square-wave injection method according to the injection signal form. Compared with the HF sinusoidal signal injection method, the HF square-wave signal injection method has the advantage of higher injection frequency, which can reach the maximum half of the switching period. In addition, the HF square-wave signal injection method is more convenient for extracting the position error, which is convenient to be applied to the actual control system. In [16,17], a hybrid sensorless control method combining the HF injection method and the active flux linkage method was proposed to cover the speed range from zero speed to rated speed. In [14], the same method of HF voltage injection was used to improve low-speed performance.

The HF signal injection method has negative impacts on SynRM drives, such as injection noise. In addition, the serious cross-saturation effect of the SynRM will affect the operation of sensorless control. To solve the noise problem, there are three main methods: amplitude adjustment, frequency adjustment and random signal injection [18–21]. Reducing the injection voltage amplitude is the most direct way to reduce the HF noise. In [22], the current oversampling method was proposed to improve the signal-to-noise ratio of the sensorless control system. However, it requires additional calculations using FPGA, which increases the system cost. The frequency regulation method of injection signal is mainly divided into two kinds: One is to use a higher injected frequency to make it beyond the range of human ear hearing. The second is to use a lower injected frequency to reduce the sharpness of audible noise, which is similar to the amplitude adjustment method. In [18], a method based on low-frequency pulse voltage injection was proposed. But it increases the complexity, and the low-frequency injection will interrupt the vector control, affecting the vector operation process. In addition, it is difficult to select the frequency and amplitude of the injected signal. If the injected signal frequency is too low, it may increase the rotor position error [23]. The power spectral density (PSD) analysis is an important method to verify the effect of noise reduction. The random HF signal injection method can suppress the discrete component in the current PSD and make it evenly distributed to reduce noise. The method disperses and widens the high-frequency noise, making the noise from sharp and harsh to low and hoarse, which can achieve the effect of reducing the noise without affecting the control accuracy. In [24], the PSD of HF current in three different schemes was compared and analyzed: fixed-frequency HF signal injection, full-period switched random frequency injection and half-period switched random frequency injection. The half-period switched random frequency injection has a better continuous PSD spectrum and better noise-reduction effect. However, the adjustment amplitude and frequency will affect the accuracy of the position observer, which generally requires additional algorithms to compensate. For random signal injection, random numbers are generated, corresponding to the real-time change in injection frequency, amplitude or phase. Then, the effect of two or more signal injections can be achieved, broadening the current power spectral density. Finally, the effect of reducing noise can be achieved without affecting the estimation accuracy.

Due to the significant cross-saturation effect of the SynRM, the sensorless estimation accuracy would be reduced. Generally, the cross-saturation effect will be more severe as the load becomes heavier. Compensating the position estimation error caused by the cross-saturation effect is especially important. There are many ways to suppress cross-saturation effects in the SynRM, including feedback control, feedforward control and model-based control. The feedback control method uses the speed and position measured by the motor to adjust the current vector to suppress the cross-saturation effect. The feedforward control method uses a predetermined torque reference value to compensate for the cross-coupled torque. Model-based control methods use a mathematical model of the motor to predict and compensate for cross-saturation torques. In addition, it can also be divided into off-line or on-line methods. Off-line measurement methods mainly use the finite-element analysis, the q-axis current factor and the lookup table. In [25], a

program based on finite element analysis was studied to correct the inductance of the SynRM model under different load conditions. The calculation method of the SynRM inductance, including cross magnetization and iron loss, was discussed in [26]. Using the equivalent circuit model representing the inductance variation in the *d*-axis and *q*-axis, the appropriate motor equation was derived. Through calculations and experiments, the motor parameters suitable for calculation were obtained. In [27], the *q*-axis current factor obtained off-line was used to compensate for the estimated position error, simplifying the implementation process, but it needs to be measured under different working conditions. In [28], structured neural networks and lookup tables were used to effectively compensate for the salience caused by saturation and improve the sensorless control performance. Due to the complexity of operating conditions, the generality of off-line measurement methods is limited. These methods have some limitations such as large computation and difficult implementation, so it is of great significance to continue to study how to suppress the cross-saturation effect.

In order to solve the problem of HF injected noise and inhibit the adverse effects of the cross-saturation effect to improve the sensorless estimation accuracy, this paper proposes a variable-angle random HF voltage injection strategy with cross-saturation effect compensation for sensorless SynRM drives. To reduce the noise generated by the HF signal injection method, a random injection method based on a chaotic map is proposed. The generation of random sequences using the chaotic mapping method is more uniform than the traditional linear congruence method, has better ergodicity and then produces better noise-reduction performance. By randomly injecting voltage signals of different frequencies, the distribution of current power spectral density is broadened and the HF noise is reduced. A cross-saturation effect suppression algorithm based on variable-angle injection is proposed. The error curves of the estimated position under different load conditions are measured off-line, and the polynomial fitting is performed. The angle of the injected signal is changed in real time according to the load conditions so that the cross-saturation effect can be suppressed. Moreover, the control accuracy and robustness can be maintained without additional hardware resources and have better realizability. Finally, the sensorless performance test based on HF voltage injection is carried out on a 3 kW SynRM experimental platform. The experimental results show that the proposed method can effectively suppress the estimated position error caused by the cross-saturation effect and has a good noise-reduction effect.

2. Proposed Random High-Frequency Square-Wave Voltage Injection-Based Sensorless Control Strategy

2.1. Proposed Random Injection Scheme

Figure 1 shows the reference frames of the SynRM, where α-β, d-q, $\hat{d}$-$\hat{q}$, d^m-q^m, d'-q' and $\bar{d}$-$\bar{q}$ axes indicate the stationary frame, the rotor frame, the estimated rotor frame, the measured frame, the inductance anisotropic coordinate system and the variable-angle injection coordinate system, respectively. θ_{err} represents the position tracking error between the actual position, θ_e, and the estimated one, $\hat{\theta}_e$, i.e., $\theta_{err} = \theta_e - \hat{\theta}_e$. When the speed is low and the injection amplitude is large, the voltage equation in d-q axis can be expressed as

$$\begin{bmatrix} u_{dh} \\ u_{qh} \end{bmatrix} = \begin{bmatrix} L_{dh} & L_{dqh} \\ L_{dqh} & L_{qh} \end{bmatrix} \mathrm{p} \begin{bmatrix} i_{dh} \\ i_{qh} \end{bmatrix}, \tag{1}$$

where $u_{dh,qh}$, $i_{dh,qh}$, $L_{dh,qh}$ are the HF voltages, currents and inductances of the *d*-axis and *q*-axis, respectively. L_{dqh} is the HF mutual inductance between the *d*-axis and *q*-axis. p is the differential operator.
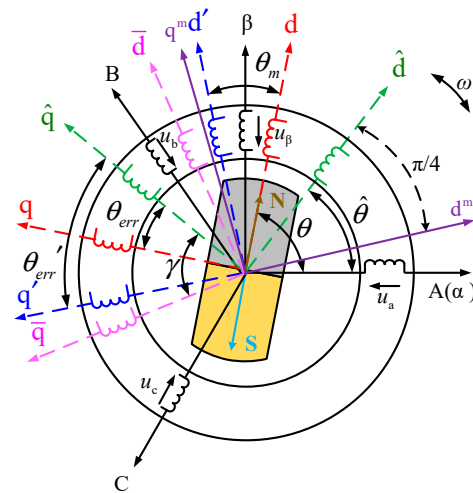
Figure 1. Reference frames of sensorless SynRM drives.

After the coordinate transformation, (1) is transformed to the d'-q' axis, which can be expressed as

$$\begin{bmatrix} u_{dh}{}^m \\ u_{qh}{}^m \end{bmatrix} = \begin{bmatrix} L_1 - L_2' \sin(2\theta_{err} + \theta_{mh}) & -L_2' \cos(2\theta_{err} + \theta_{mh}) \\ -L_2' \cos(2\theta_{err} + \theta_{mh}) & L_1 + L_2' \sin(2\theta_{err} + \theta_{mh}) \end{bmatrix} \cdot p \begin{bmatrix} i_{dh}{}^m \\ i_{qh}{}^m \end{bmatrix}, \quad (2)$$

where $u_{dh}{}^m$, $_{qh}{}^m$, $i_{dh}{}^m$ and $_{qh}{}^m$ are the voltages and currents of the d-axis and q-axis under d'-q' axis, respectively. $L_1 = (L_{dh} + L_{qh})/2$, $L_2 = (L_{dh} - L_{qh})/2$, $\theta_{mh} = \arctan[2L_{dqh}/(L_{dh} - L_{qh})]$, $L_2' = \sqrt{L_2{}^2 + L_{dqh}{}^2}$.

Figure 2 shows the random HF square-wave voltage injection-based sensorless control block diagram. On the basis of HF square-wave injection, a random HF signal generator is added to inject random signals. It is used to generate four different square waves for random injection. The random signal generator is composed of a random number generator, comparator and signal selection. A series of random numbers are generated by the random number generator. The range of the generated random numbers is judged by the comparator to select the corresponding injection signal. Then, the HF voltage signal with varying frequencies is generated. The random HF signal generator can be expressed as

$$u_k = \begin{cases} U_k, t \in \left[nT_k, \left(n + \tfrac{1}{2}\right)T_k\right] \\ -U_k, t \in \left[\left(n + \tfrac{1}{2}\right)T_k, (n+1)T_k\right] \end{cases}, \ k = 1, 2, 3, 4, \quad (3)$$

where u_k is the injected voltage with amplitude U_k and T_k denotes the HF injection period for the single-axis injection. T_k and U_k choose different values that correspond to four different frequencies of the signal. In order to ensure that the excitation current signal amplitudes generated by signals of different frequencies are equal, the value must satisfy

$$U_k T_k = C, \, k= 1, 2, 3, 4, \quad (4)$$

where C is constant.

The HF signal is injected into d'-q' axis

$$\begin{bmatrix} u_{dh}{}^m \\ u_{qh}{}^m \end{bmatrix} = \begin{bmatrix} u_k \\ u_k \end{bmatrix}. \quad (5)$$

Combining (2) and (5), the HF response current can be expressed as

$$p \begin{bmatrix} i_{dh}{}^m \\ i_{qh}{}^m \end{bmatrix} = \frac{u_k}{L_1{}^2 - L_2'{}^2} \cdot \begin{bmatrix} L_1 + L_2' \sin(2\theta_{err} + \theta_{mh}) + L_2' \cos(2\theta_{err} + \theta_{mh}) \\ L_1 - L_2' \sin(2\theta_{err} + \theta_{mh}) + L_2' \cos(2\theta_{err} + \theta_{mh}) \end{bmatrix}. \quad (6)$$

The position information is obtained with a position tracking observer forcing θ_{err} to zero. When θ_{err} is very small, (6) can be simplified to

$$\text{p}i_{dh}{}^m \approx \frac{u_k}{L_1{}^2 - L_2{'}^2}[L_{dh} + L_{dqh} + (L_{dh} - L_{qh} - 2L_{dqh})\cdot\theta_{err}]. \tag{7}$$

$$\text{p}i_{qh}{}^m \approx \frac{u_k}{L_1{}^2 - L_2{'}^2}[L_{dh} - L_{dqh} + (L_{qh} - L_{dh} - 2L_{dqh})\cdot\theta_{err}]. \tag{8}$$
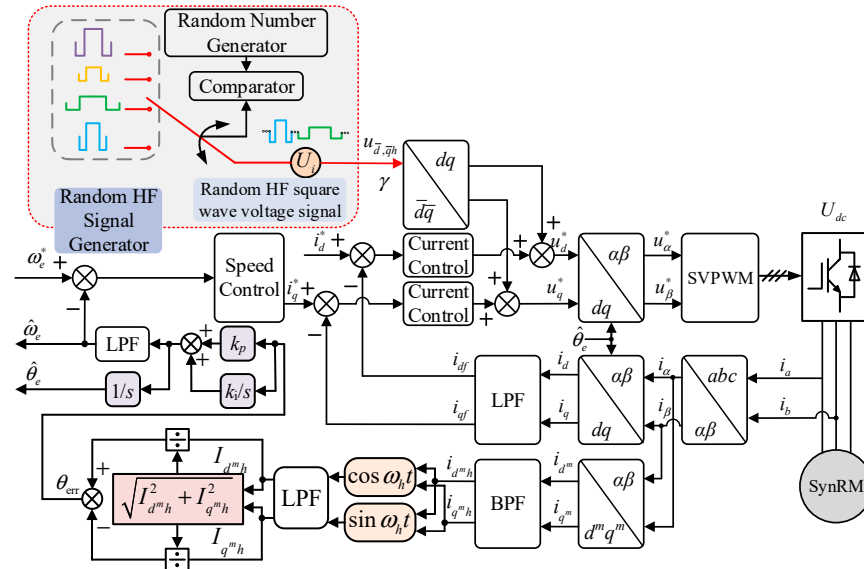

Figure 2. Block diagram of random HF square-wave voltage injection-based sensorless control system.

Multiplying (7) by $\lambda = \frac{L_{dh} - L_{dqh}}{L_{dh} + L_{dqh}}$ and subtracting (8), it can be obtained as

$$\text{p}(i_{qh}{}^m - \lambda i_{dh}{}^m) = \frac{u_k}{L_1{}^2 - L_2{'}^2}\cdot\frac{2L_{dh}L_{qh} - 2L_{dh}{}^2 - 4L_{dqh}{}^2}{L_{dh} + L_{dqh}}\cdot\theta_{err}. \tag{9}$$

Then, by adjusting (9) to zero through the PI observer, the rotor position information can be obtained. The HFSI-based method is well suited for an interior permanent magnet synchronous motor (IPMSM) and the SynRM due to the large spatial saliency. For a surface permanent-magnet synchronous motor (SPMSM), the dependence of the spatial inductance distribution on the rotor position is weak; however, the spatial saliency can be related to the saturation effect of the stator leakage flux or main flux [29,30]. Therefore, the HFSI-based method is also suitable for an SPMSM.

2.2. Chaotic Mapping Method-Based Random Number Generation Principle

After four square-wave signals of different frequencies are generated, a random number needs to be generated, and the type of injected signal is determined according to the value of the random number. From the random signal generator block diagram in Figure 2, the random number generator generates a random sequence of numbers. The comparator judges the range of the generated random numbers and selects the corresponding injection signal. Then, it generates the HF voltage signal when the frequency changes.

The linear congruence method is a pseudorandom number generation algorithm that produces a series of seemingly random numbers. The principle is to give an initial value, through a series of calculations obtain the next random number, and then use this random number as the initial value of the next calculation, so reciprocating to generate a random series of numbers [31]. The expression of the linear congruence method is

$$Z_{i+1} = (AZ_i + B)\text{mod}M, \tag{10}$$

where *A* is the multiplier, *B* is the increment and *M* is the mod.

This gives a random number evenly distributed over the interval (0, 1). The linear congruence method is still widely used because of its few parameters and simple calculation. However, due to the limitation of microprocessor data bits, the sequence period generated by this method cannot be large, so its randomness is limited.

Chaos is a disordered, complex and unpredictable phenomenon in nonlinear dynamic systems. In such systems, small changes in initial conditions can lead to large changes in the evolution of the system, making the outcome unpredictable. Chaos has the advantages of high randomness, nonlinear characteristics, stability, high efficiency, controllability and easy implementation, which makes it suitable for the generation of random numbers. The chaotic mapping method is used to generate random numbers. Logistic mapping is one of the most widely used models in chaotic systems, which can be expressed as

$$x_{n+1} = rx_n(1 - x_n), \tag{11}$$

where $x(n)$ represents the value on the nth iteration.

The iterative process of logistic mapping is very simple and only needs to be iterated using (10). Because of its simplicity and controllability, logistic mapping is widely used in random number generation, data encryption, image encryption, chaotic modulation and other fields. In (10), only when $0 < x_n < 1$ and $3.569949 < r < 4$, logistic mapping can produce chaos. When r is not in the above range, (10) does not produce chaos. However, for other complex chaotic mapping systems, this judgment method is inconvenient to use. Therefore, the maximum Lyapunov index is used to judge chaos:

$$\lambda(x_0) = \lim_{n \to \infty} \frac{1}{n} \sum_{i=0}^{n-1} \ln|f'(x_n)| = \int_0^1 \rho(x) \ln|f'(x_n)| dx, \tag{12}$$

with

$$\rho(x) = \begin{cases} \frac{1}{\pi\sqrt{x(1-x)}} & ,0 < x < 1 \\ 0 & ,\text{other} \end{cases}. \tag{13}$$

When the maximum Lyapunov index is greater than zero, (10) will be chaos. Figure 3 is the maximum Lyapunov index value at different values of r. It can be seen that when r is less than 3.58, the maximum Lyapunov index is less than zero, and it is in a non-chaotic state. The result is also verified by the bifurcation diagram in Figure 4 when r takes different values.
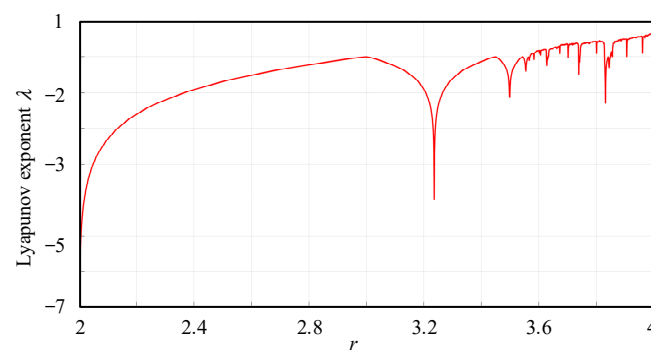

Figure 3. Maximum Lyapunov exponent plot with different r values.
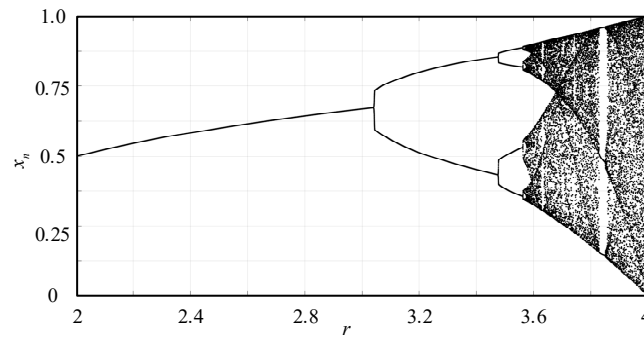
Figure 4. Bifurcation diagram with different *r* values.

The expression of generating a random sequence of numbers with uniform probability density by using integer chaotic mapping is

$$
Z_{i+1} =
\begin{cases}
m\{[NZ_i - D(j-1)], \mu(Dj - NZ_i)\}, \\
\frac{Z_i}{D} \in \left[\frac{j-1}{N}, \frac{j}{N}\right] \\
D - m\{(NZ_i - Dj), \mu[D(i+1) - NZ_i]\}, \\
\frac{Z_i}{D} \in \left[\frac{j}{N}, \frac{j+1}{N}\right]
\end{cases} ,
\tag{14}
$$

where N is the number of segments. μ is the controls parameter. D indicates the maximum value of the data, which is usually $2^P - 1$. J is the break sign, $j = 1, 3, 5, \ldots, N - 3, N - 1$. $R_i = Z_i/D$.

Due to the limited computing power of the microprocessor, a large number of real number operations affect the algorithm running speed. In order to solve the above problems, segmental logistic mapping is integer-processed. Since the integer-piecewise logistic map converts the real value to the integer value, the integer operation is more efficient than the real number operation, which can significantly improve the calculation speed. Because of the use of integer operation, integer-piecewise logistic mapping has stronger stability, which can avoid the problem of random number instability caused by calculation errors. In this way, random numbers are uniformly distributed in the interval $(0, 1)$. The problem of precision loss when chaotic systems are represented by floating point numbers is eliminated by using integers. Taking $\mu = 4$, $N = 64$, $p = 64$, the maximum Lyapunov index at this time is calculated as 0.127, indicating that the system is chaotic. Finally, according to the different values of R_i, different injection signals are selected as shown in (14).

$$
k =
\begin{cases}
1, R_i \in [0, 0.25] \\
2, R_i \in [0.25, 0.5] \\
3, R_i \in [0.5, 0.75] \\
4, R_i \in [0.75, 1.0]
\end{cases} .
\tag{15}
$$

The power density spectrum analysis of the SynRM phase current is an important method to judge whether the noise-reduction effect is effective. The random HF square-wave voltage injection method can effectively reduce the discrete components in current phase PSD and make the spectrum distribution more uniform:

$$
S(f) = \frac{1}{T_i}
\left\{
\begin{array}{l}
\mathrm{E}\left[\left|I(f)^2\right|\right] - \mathrm{E}[|I(f)|]^2 \\
+ T_i |\mathrm{E}[I(f)]|^2 \sum\limits_{k=-\infty}^{+\infty} \delta(f - \frac{k}{T_i})
\end{array}
\right\} ,
\tag{16}
$$

where E [] is the mathematical expectation operator. $\delta()$ is the impulse equation. $I(f)$ is the Fourier transform of current. T_i is the period of injection signal.

If injecting four square-wave signals completely at random, that is $p_1 = p_2 = p_3 = p_4 = 0.25$, $\mathrm{E}[I(f)]$ can be kept constant at 0 and the discrete spectral component is 0. There are only

continuous spectral components in phase current PSD, which can effectively reduce the HF noise caused by the presence of discrete spectrum.

Different random number generation methods have almost the same resource usage. The uniformity of the two algorithms is compared below. The generated 10,000 random numbers are divided into 200 distribution areas on (0, 1), and the probability density distribution map is obtained, as shown in Figure 5. The random number uniformity generated by the linear congruence method is not satisfactory enough: the probability density fluctuates greatly, ranging from 0.66 to 1.41. The random number generated by the chaotic mapping method has good uniformity: the probability density fluctuates between 0.85 and 1.23, and the fluctuation is smaller. Therefore, through the performance analysis of the two random number generators, it is found that the ergodicity of the two methods is good, and the entire interval can be traversed. However, the uniformity of the chaotic mapping method is better.
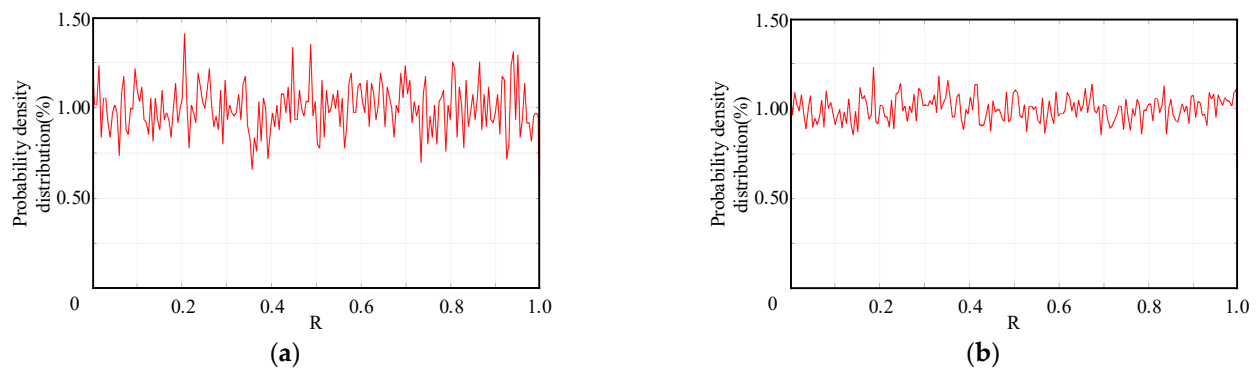

Figure 5. Uniformity comparison of the two algorithms. (**a**) Probability density distribution of linear congruence method. (**b**) Probability density distribution of chaotic mapping method.

3. SynRM Cross-Saturation Effect Suppression Algorithm Based on Variable-Angle Injection

3.1. Analysis of Position Error Caused by Cross-Saturation

When the cross-saturation effect is ignored, (1) can be converted to (17).

$$\begin{bmatrix} u_{dh} \\ u_{qh} \end{bmatrix} = \begin{bmatrix} L_{dh} & 0 \\ 0 & L_{qh} \end{bmatrix} \mathrm{p} \begin{bmatrix} i_{dh} \\ i_{qh} \end{bmatrix}. \tag{17}$$

The HF signal is injected into $\hat{d}$-$\hat{q}$ axis

$$\begin{bmatrix} u_{\hat{d}h} \\ u_{\hat{q}h} \end{bmatrix} = \begin{bmatrix} u \\ 0 \end{bmatrix}, \tag{18}$$

where $u_{\hat{d}h,\hat{q}h}$ are the voltages in $\hat{d}$-$\hat{q}$ axis. u is the injected voltage in (3) with $k = 1$.

The HF response current in d^m-q^m axis can be expressed as

$$\mathrm{p} \begin{bmatrix} i_{dh}^m \\ i_{dh}^m \end{bmatrix} = \frac{u}{\sqrt{2}(L_1{}^2 - L_2{}^2)} \begin{bmatrix} L_1 - L_2(\cos(2\theta_{err}) + \sin(2\theta_{err})) \\ L_1 - L_2(\cos(2\theta_{err}) - \sin(2\theta_{err})) \end{bmatrix}. \tag{19}$$

Subtracting i_{dh}^m and i_{qh}^m to obtain

$$\mathrm{p}(i_{dh}^m - i_{dh}^m) \approx \frac{2\sqrt{2}uL_2}{(L_1{}^2 - L_2{}^2)} \cdot (\theta_{err}' - \theta_m), \tag{20}$$

where θ_{err}' is the true position estimation error and $\theta_{err} = \theta_{err}' - \theta_m$.

The rotor position observer converges $\theta_{err}{}'$ to θ_m, instead of converging to 0. Therefore, a position error θ_m due to the cross-saturation effect is generated, which varies with inductance parameters. θ_m can be expressed as

$$\theta_m = \frac{1}{2}\arctan\frac{2L_{dqh}}{L_{qh} - L_{dh}}. \tag{21}$$

The self-inductance and mutual inductance of the SynRM will change under different magnetic field conditions, according to (20). It can be seen that θ_m will change with the change in self-inductance and mutual inductance. So, the variational angle error between the estimated frame and the actual frame will occur, which is the cause of the estimation position error. Since Equation (20) has three independent variables, it is difficult to analyze the relationship between the variables. Therefore, simulation software is used to fix one of the variables and draw a figure in which the position error changes with the other two variables. It can be seen from Figure 6:

(1) When L_{dh} is fixed, θ_m increases with the increase in L_{dqh} and decreases with the increase in L_{qh}. θ_m changes significantly when L_{dqh} is small and tends to be stable when L_{dqh} is large.

(2) When L_{qh} is fixed, θ_m increases with the increase in L_{dqh} and increases with the increase in L_{dh}.

(3) When L_{dqh} is fixed, the change in θ_m is less obvious. θ_m increases with the increase in L_{dh} and decreases with the increase in L_{qh}.
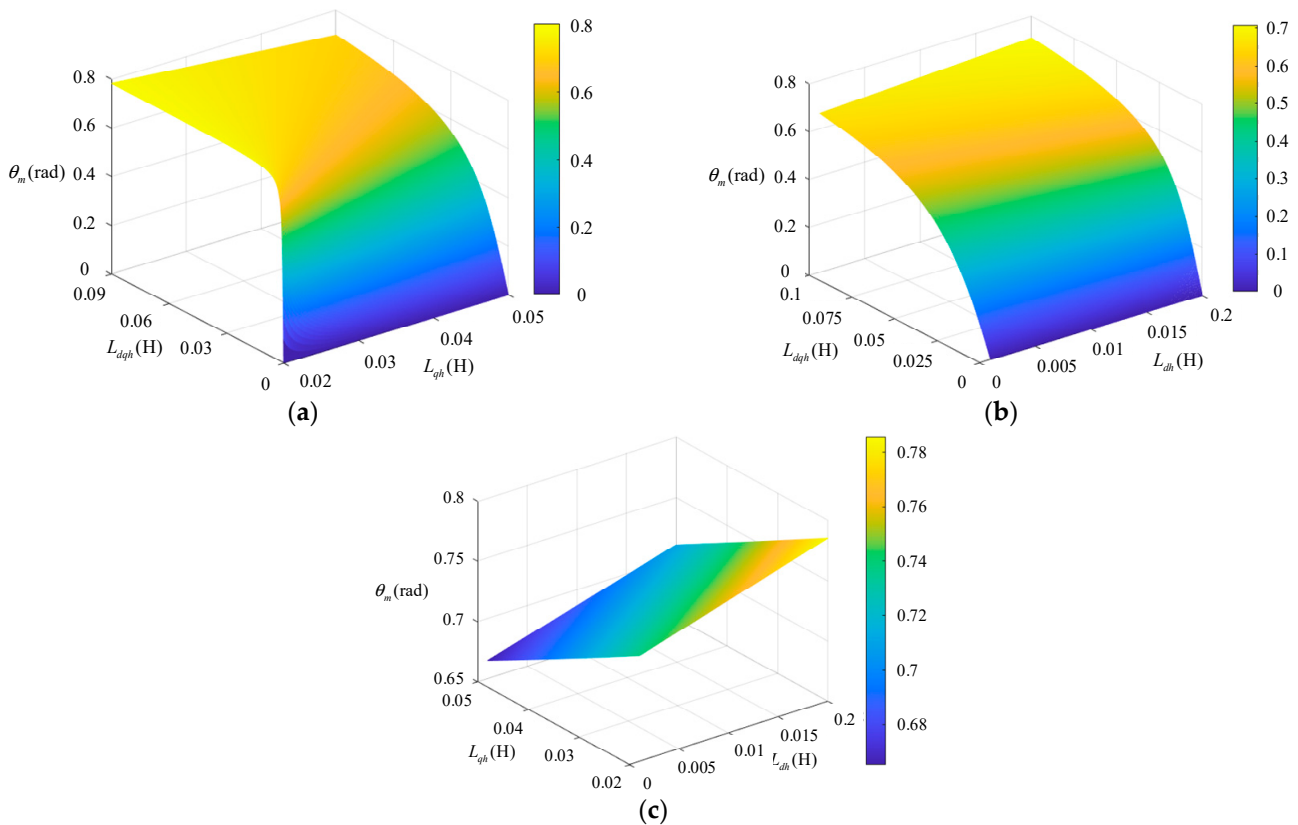

Figure 6. Position error and inductance relation plot. (**a**) Fixed L_{dh}. (**b**) Fixed L_{qh}. (**c**) Fixed L_{dqh}.

From (20), the comprehensive analysis of the three figures in Figure 6 shows that the maximum position error value is about 0.8 rad, which has a great impact on the stable operation. Therefore, the influence of cross-saturation effect cannot be ignored, and it needs to be compensated. The relation between inductance and current is nonlinear because of

the cross-saturation effect, so it is difficult to obtain a specific and accurate inductance value by the parameter identification method.

3.2. Variable-Angle Square-Wave Injection with Cross-Saturation Effect Compensation

The variable-angle injection control method is based on random HF square-wave injection control; adding a variable-angle inverse park transform, the inverse park transform angle is γ. Angle-variable control is realized by adjusting the angle in real time. First, the square-wave signal is injected into the $\bar{d}$-$\bar{q}$ axis, which differs from $\hat{d}$-$\hat{q}$ by γ.

$$\begin{bmatrix} u_{\bar{d}h} \\ u_{\bar{q}h} \end{bmatrix} = \begin{bmatrix} u \\ 0 \end{bmatrix}. \tag{22}$$

Combining (1) and (21), the current can be simplified to

$$\mathrm{p}(i_{d^m h} - i_{d^m h}) \approx \frac{2\sqrt{2}uL_2{}'}{(L_1{}'^2 - L_2{}'^2)} \cdot (\theta_{err}{}' - \theta_m - \gamma), \tag{23}$$

where $L_1{}' = \frac{L_{Dh} + L_{Qh}}{2}$, $L_2{}' = \frac{L_{Dh} - L_{Qh}}{2}$.

If the injection angle is set to $\gamma = -\theta_m$, (22) can be expressed as

$$\mathrm{p}(i_{d^m h} - i_{d^m h}) \approx \frac{2\sqrt{2}uL_2}{(L_1{}'^2 - L_2{}'^2)} \cdot (\theta_{err}{}'). \tag{24}$$

The amplitude of the HF current information can be obtained by LPF.

$$\begin{cases} I_{d^m h} = 2\sqrt{\left[LPF\left(\frac{1}{2}\cos\omega t \cdot i_{d^m h}\right)\right]^2 + \left[LPF\left(\frac{1}{2}\sin\omega t \cdot i_{d^m h}\right)\right]^2} \\ I_{q^m h} = 2\sqrt{\left[LPF\left(\frac{1}{2}\cos\omega t \cdot i_{q^m h}\right)\right]^2 + \left[LPF\left(\frac{1}{2}\sin\omega t \cdot i_{q^m h}\right)\right]^2} \end{cases}. \tag{25}$$

Then, the $\theta_{err}{}'$ can be obtained by LPF and standard processing.

$$I_{d^m h}^* - I_{q^m h}^* = \frac{I_{d^m h} - I_{q^m h}}{\sqrt{I_{q^m h}^2 + I_{d^m h}^2}} \approx \theta_{err}{}'. \tag{26}$$

By adjusting the $\theta_{err}{}'$ to zero through the PI observer, the rotor position information can be obtained as shown in Figure 2, so that the position error caused by the cross-saturation effect can be eliminated and the high-performance control of the system can be achieved.

The variable angle is measured off-line, obtained by experimental measurement and curve fitting, and approximated by the position error angle in (23). The method does not need to accurately measure the inductance value, but only needs the estimated position error under different load conditions to compensate for the cross-saturation effect. Figure 7 is the position error diagram under different load conditions. As can be seen, the position error and load torque are non-linear, and the position error gradually increases with the increase in the load.

Figure 8 uses the polynomial fitting method to fit the position error. As can be seen, the fitting results of cubic polynomial are more accurate than that of quadratic polynomial and can fit data points better. Therefore, the cubic polynomial fitting results are used in the experiment. The quadratic polynomial fitting formula is shown in (24) and cubic polynomial fitting formula is shown in (25):

$$y = 2.27 \times 10^{-5}x^2 + 3.10 \times 10^{-4}x + 4.32 \times 10^{-2}, \tag{27}$$

$$y = 5.36 \times 10^{-7}x^3 - 5.77 \times 10^{-5}x^2 + 3.38 \times 10^{-3}x + 2.39 \times 10^{-2}, \tag{28}$$

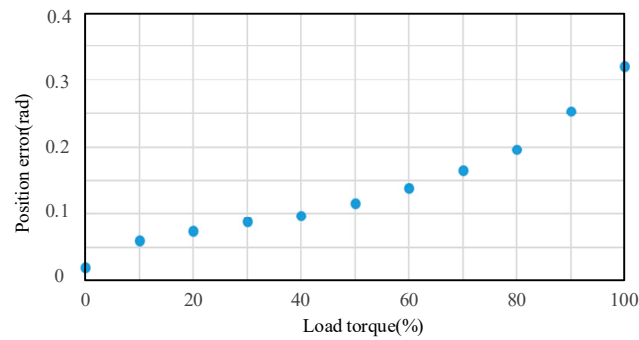where y is the position error and x is the load torque.

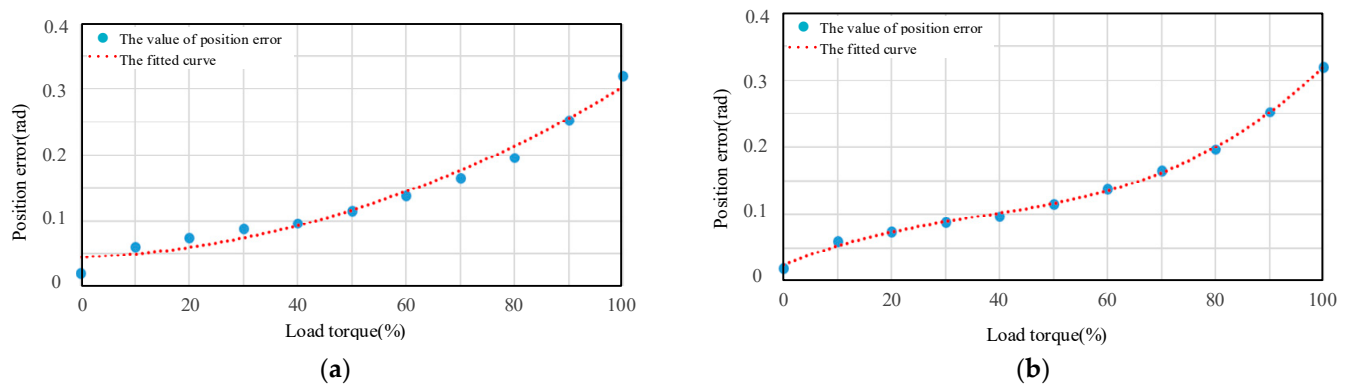**Figure 7.** Position error diagram under different load conditions.

Figure 8. Polynomial fitting result plot. (**a**) Quadratic polynomial fitting. (**b**) Cubic polynomial fitting.

4. Experimental Results

The proposed control strategy was verified on a 3 kW SynRM drive as shown in Figure 9 and the parameters are shown in Table 1. The hardware structure of the drive system is mainly composed of rectifier, inverter, current detection, auxiliary power supply, position sensor acquisition module, digital-to-analog conversion module and so on. The sampling frequency and PWM switching frequency was 10 kHz. Absolute encoders were used to obtain real rotational speed and rotor position information to verify the accuracy of the sensorless control method. The control algorithm of variable-angle random HF voltage injection strategy with cross-saturation effect compensation for sensorless SynRM drives was implemented in the STM32F103VCT6. The flow chart of the whole control system is shown in Figure 10.
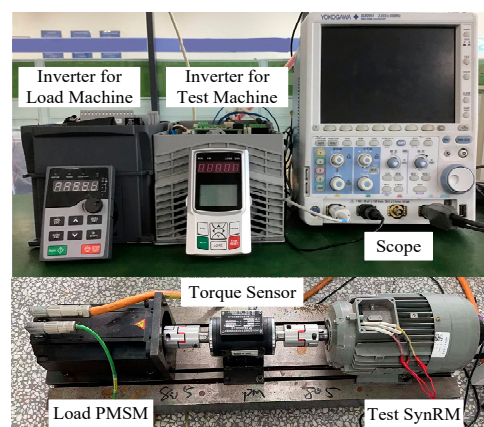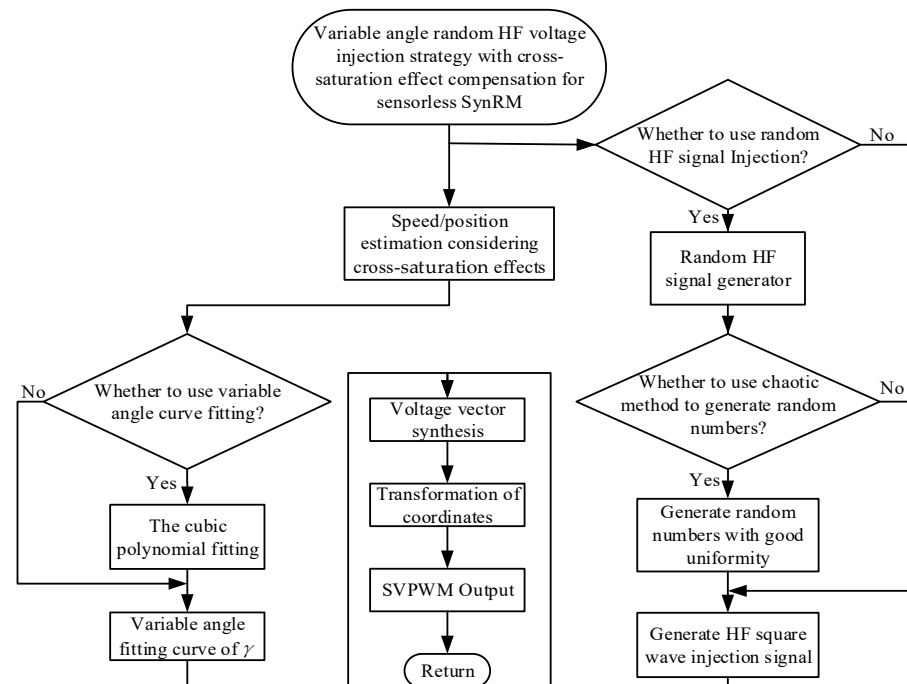

Figure 9. 3 kW SynRM experimental platform.

Table 1. The parameters of SynRM.

Electric Machine Parameter	Value
Rated power (kW)	3
Rated current (A)	7.6
Rated voltage (V)	360
Rated speed (r/min)	3000
Phase resistance (Ω)	0.524
d-axis inductance (mH)	51
q-axis inductance (mH)	19
Pairs of poles	2

Figure 10. The flow chart of the proposed method.

Firstly, the steady-state performance of sensorless control for the SynRM drive based on random HF voltage injection was tested. The experimental waveform from top to bottom is estimated position, estimated position error and a-phase current. As can be seen from Figure 11, the motor can run stably from 0 r/min to 750 r/min. The estimated position waveform was smooth and stable without obvious mutation. The estimated position error pulsation was small, and the phase current waveform was smooth and stable. The maximum error of the estimated position was 0.13 rad. Therefore, the experimental results show that the proposed method can make the SynRM run stably and restrain the cross-saturation effect well.

Different signal injection methods are comparatively evaluated in Figure 12 with the tested SynRM running at 300 r/min with 100% rated load torque. As can be seen, when the motor ran at 300 r/min with 100% rated load torque, the SynRM ran stably under different signal injection methods, and the rotor position was estimated accurately. In addition, the zoomed-in phase current and torque ripple are also comparatively illustrated in Figure 12. Also, the HF current component can be observed from the zoomed-in phase current. The experimental results show that the random signal was injected into the system and had no effect on the stable operation of the system. The proposed method does not increase the torque ripple and can run stably. In addition, it is worth noting that the proposed variable-angle random injection could effectively compensate the cross-saturation effect induced estimated position error compared with the conventional cross-saturation factor method [32].
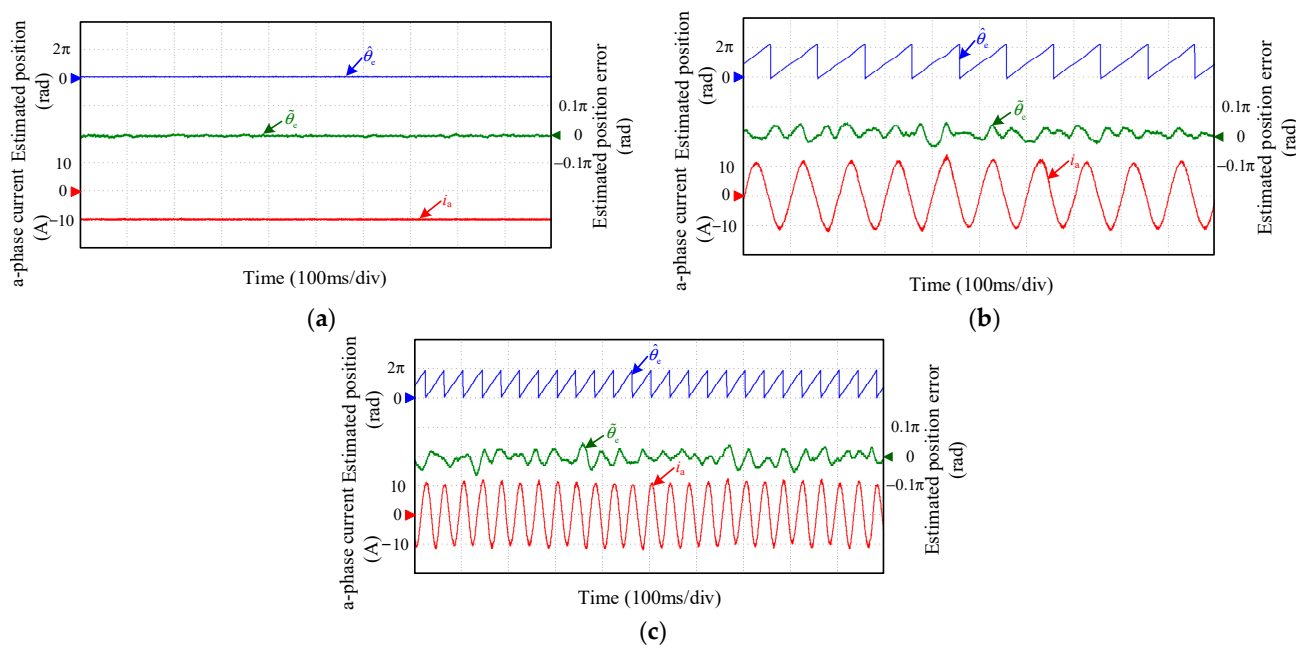
Figure 11. Steady-state operation experimental results with 100% rated load. (**a**) At 0 r/min. (**b**) At 300 r/min. (**c**) At 750 r/min.
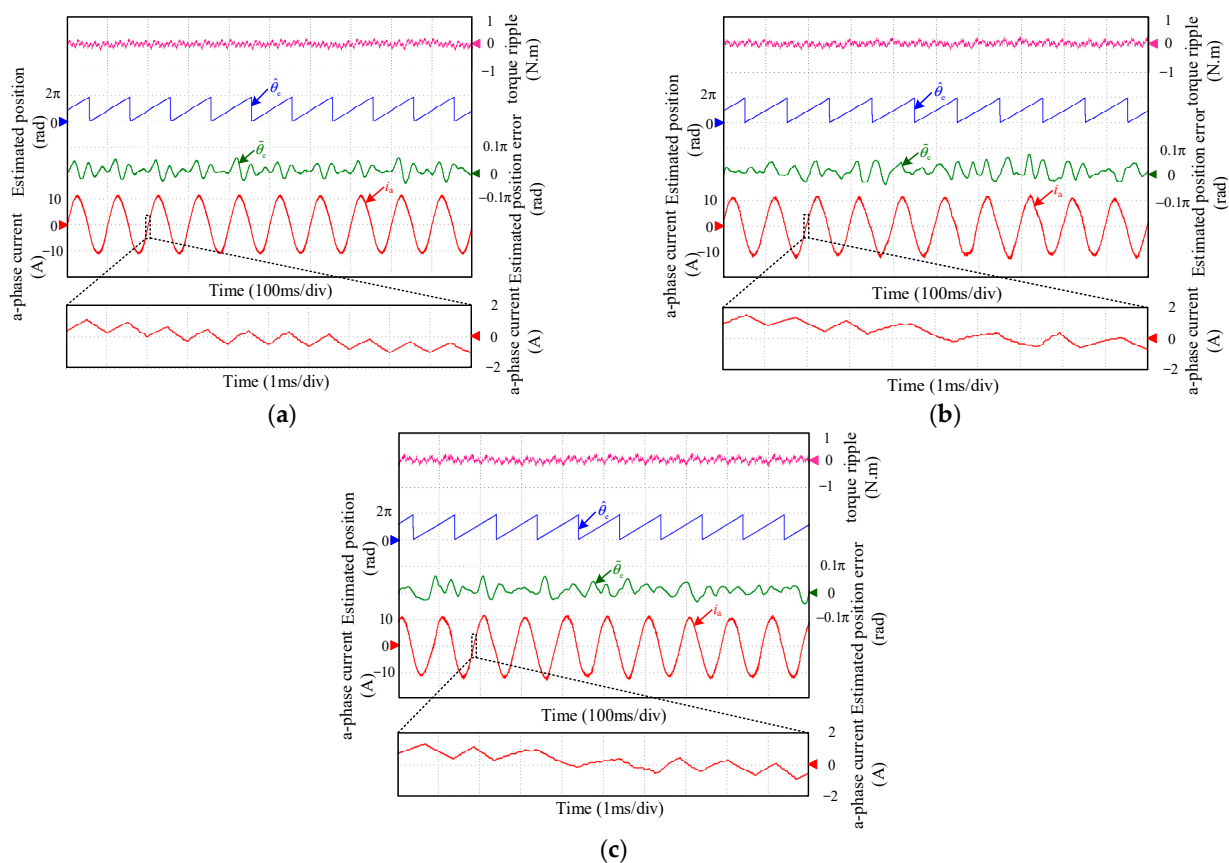

Figure 12. Different injection methods experimental results with 100% rated load. (**a**) Fixed frequency. (**b**) Random injection using linear congruence method. (**c**) Random injection using chaotic mapping method.

Figure 13 shows the PSD analysis diagram of fixed-frequency signal injection and random injection phase current with 100% rated load torque. It can be seen that the power

density spectrum of random injection was flat without obvious spikes at 2.5 kHz, 5 kHz and 7.5 kHz. Compared with the fixed-frequency injection, the maximum reduction was 37 dB at double injected frequency (2.5 kHz) and 32 dB at triple injected frequency (7.5 kHz). The validity of random injection algorithm based on chaotic mapping was verified.
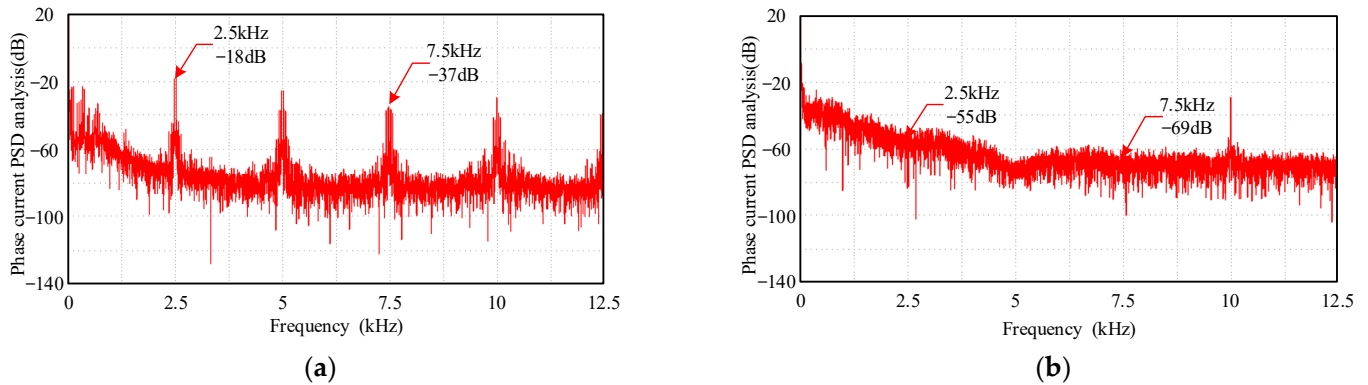

Figure 13. Steady-state operation experimental results of phase current PSD test with 100% rated load at 600 r/min. (**a**) Fixed-frequency injection. (**b**) Random injection.

Figure 14 is the experimental results of sudden increase and decrease of 100% rated load torque at 0 r/min and 300 r/min. The experimental waveform from top to bottom is actual speed, estimated position error and a-phase current. The motor ranstably when it is running without load, and the estimated position error was maximum 0.30 rad. When the load torque suddenly increases to 100% rated torque, the speed dropped transitorily, but the speed recovered after 200 ms. So, when the proposed method is used, the system has a good dynamic response. The estimated position error increased slightly, but it still fluctuated around 0 rad. After removing the load, the speed increased slightly and quickly recovered to the given speed. The estimated position error was still around 0 rad. There is no bias of the estimated position error on the whole, which proves that the proposed sensorless control algorithm can better suppress the estimated rotor position error caused by the cross-saturation effect of the SynRM.
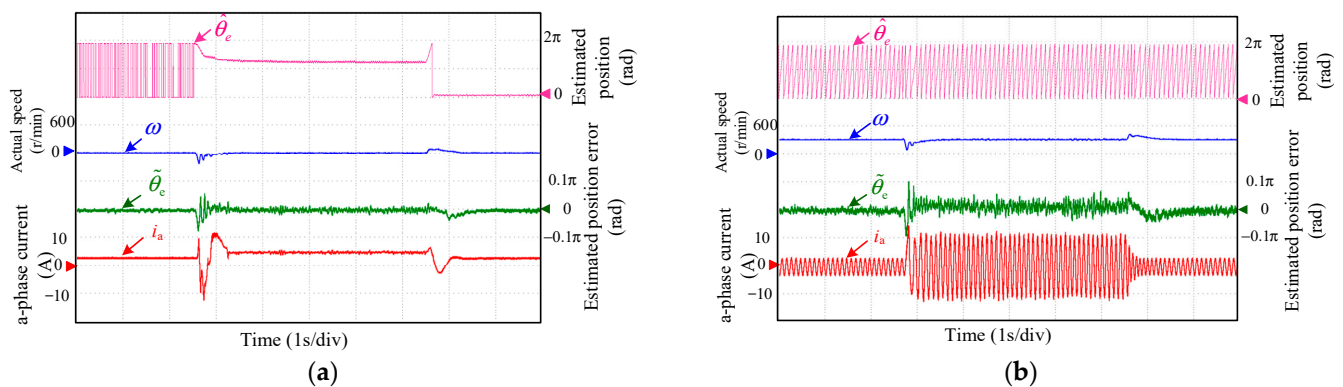

Figure 14. Experimental results of sudden increase and decrease of 100% rated load torque. (**a**) At 0 r/min. (**b**) At 300 r/min.

Figure 15 is the experimental results of acceleration and deceleration with 100% rated load. The experimental waveform from top to bottom is actual speed, estimated position error and a-phase current. It can be seen that the motor ran stably under 100% rated load condition with smooth current and no obvious mutation. The estimated position error fluctuated around 0 rad with a maximum of 0.30 rad. According to Figure 15a, the actual speed changed stably with speed fluctuation within 60 r/min. According to Figure 15b, the actual speed changed stably with speed fluctuation within 70 r/min. The estimated

position error ripple increased when accelerating or decelerating, but it still fluctuated around 0 rad and soon restored the same as the steady state operation. Experimental results show that the proposed method can run stably under acceleration and deceleration conditions and has good dynamic performance.
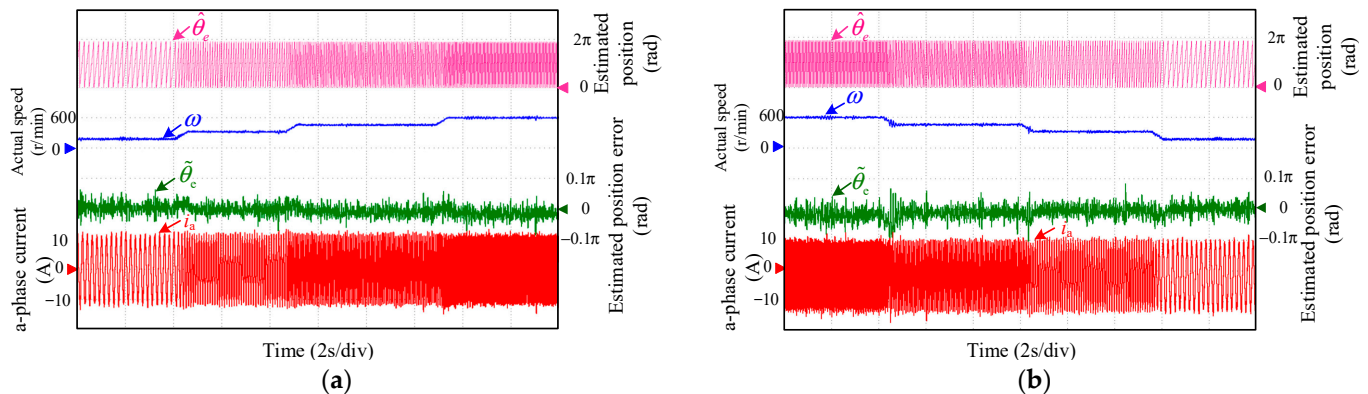

Figure 15. Experimental results of acceleration and deceleration with 100% rated load. (**a**) Acceleration (150–300–450–600 r/min). (**b**) Deceleration (600–450–300–150 r/min).

5. Conclusions

This paper proposes a variable-angle random HF voltage injection strategy with cross-saturation effect compensation for sensorless SynRM drives. Firstly, the position observation error of sensorless control algorithm based on HF injection is analyzed due to the cross-saturation effect. By randomly injecting voltage signals of different frequencies generated by chaotic mapping, the method reduces the HF noises. To suppress the estimated position error caused by the cross-saturation effect, the variable-angle injection strategy, which can change the injection angle in real time according to the load conditions, was proposed. In addition, the control accuracy and robustness can be maintained without additional hardware resources and has better realizability and practicability. Finally, the sensorless performance test based on variable-angle random HF voltage injection was carried out on a 3 kW SynRM experimental platform. The experimental results show that, compared with the traditional method, the proposed method can operate stably, effectively suppress the estimated position error caused by the cross-saturation effect and significantly reduce the noises. Although, the control strategy based on variable-angle square-wave injection can effectively suppress the estimated position error caused by the cross-saturation effect of the SynRM. This method requires the off-line measurement to obtain the fitted curve of the injection angle in advance, which increases the complexity. Therefore, to improve the generality, the fitted curve of injection angle and other on-line cross-saturation compensation algorithms could be further studied.

Author Contributions: Conceptualization, L.L., Z.H. and S.L. (Sisi Li); methodology, L.L. and R.G.; validation, J.W., G.W. and S.L. (Shulin Li); formal analysis, Z.H.; investigation, S.L. (Sisi Li); resources, G.W.; data curation, J.W. and S.L. (Shulin Li); writing—original draft preparation, L.L., Z.H. and S.L. (Sisi Li); writing—review and editing, R.G. and J.W.; visualization, R.G.; supervision, L.L.; project administration, G.W. and S.L. (Shulin Li); funding acquisition, R.G. All authors have read and agreed to the published version of the manuscript.

Data Availability Statement: Data are contained within the article.

References

1. Foti, S.; De Caro, S.; Scimone, T.; Testa, A.; Tornello, L.D.; Scelba, G.; Cacciato, M. Rotor Position Error Compensation in Sensorless Synchronous Reluctance Motor Drives. *IEEE Trans. Power Electron.* **2022**, *37*, 4442–4452. [CrossRef]

2. Kim, H.; Park, Y.; Oh, S.-T.; Jeong, G.; Seo, U.-J.; Won, S.-H.; Lee, J. Study on Analysis and Design of Line-Start Synchronous Reluctance Motor Considering Rotor Slot Opening and Bridges. *IEEE Trans. Magn.* **2022**, *58*, 1–6. [CrossRef]

3. Farhan, A.; Abdelrahem, M.; Saleh, A.; Shaltout, A.; Kennel, R. Robust Sensorless Direct Speed Predictive Control of Synchronous Reluctance Motor. In Proceedings of the 2020 IEEE 29th International Symposium on Industrial Electronics (ISIE), Delft, The Netherlands, 17–19 June 2020; pp. 1541–1546.

4. Deng, W.; Tang, J.; Cheng, W. An Enhanced Rotating Vector-Based Direct Torque Control for Matrix Converter-Fed PMSM Drives Using Virtual Pulsating Vectors. *CPSS Trans. Power Electron. Appl.* **2023**, *8*, 65–73. [CrossRef]

5. Yang, X.; Wang, Y.; Shen, J. MRAS sensorless control for synchronous reluctance motors. *Electr. Mach. Control.* **2019**, *23*, 1–9.

6. Guo, L.; Ma, J.; Qi, J. Model-free Predictive Current Control Strategy for Synchronous Reluctance Motor. *Electr. Drive* **2020**, *50*, 8–14.

7. Farhan, A.; Abdelrahem, M.; Shaltout, A.; Kennel, R.; Saleh, A. Encoderless Current Predictive Control of Synchronous Reluctance Motor by Extended Kalman Filter based State Estimation. In Proceedings of the PCIM Europe Digital Days 2020, International Exhibition and Conference for Power Electronics, Intelligent Motion, Renewable Energy and Energy Management, Nuremburg, Germany, 7–8 July 2020.

8. Mirazim, M.S.; Kiyoumars, A. Magnetic Field Analysis of SynRel and PMASynRel Machines with Hyperbolic Flux Barriers Using Conformal Mapping. *IEEE Trans. Transp. Electrif.* **2020**, *6*, 52–61. [CrossRef]

9. Pasqualotto, D.; Rigon, S.; Zigliotto, M. Sensorless Speed Control of Synchronous Reluctance Motor Drives Based on Extended Kalman Filter and Neural Magnetic Model. *IEEE Trans. Ind. Electron.* **2023**, *70*, 1321–1330. [CrossRef]

10. Wu, X.; Huang, S.; Liu, K.; Lu, K.; Hu, Y.; Pan, W.; Peng, X. Enhanced Position Sensorless Control Using Bilinear Recursive Least Squares Adaptive Filter for Interior Permanent Magnet Synchronous Motor. *IEEE Trans. Power Electron.* **2020**, *35*, 681–698. [CrossRef]

11. Teng, Q.; Yang, H.; Tian, J. Nonlinear Function Integral Sliding Mode-Based Model Predictive Current Control for PMSM Drives With DC-Bus Voltage Observer. *CPSS Trans. Power Electron. Appl.* **2022**, *7*, 399–408. [CrossRef]

12. Yoon, Y.-D.; Sul, S.-K.; Morimoto, S.; Ide, K. High bandwidth sensorless algorithm for AC machines based on square-wave type voltage injection. In Proceedings of the 2009 IEEE Energy Conversion Congress and Exposition, San Jose, CA, USA, 20–24 September 2009.

13. Agarlita, S.C.; Boldea, I.; Blaabjerg, F. High-Frequency-Injection-Assisted "Active-Flux"-Based Sensorless Vector Control of Reluctance Synchronous Motors, With Experiments from Zero Speed. *IEEE Trans. Ind. Appl.* **2012**, *48*, 1931–1939. [CrossRef]

14. Yousefi-Talouki, A.; Pescetto, P.; Pellegrino, G.; Boldea, I. Combined Active Flux and High-Frequency Injection Methods for Sensorless Direct-Flux Vector Control of Synchronous Reluctance Machines. *IEEE Trans. Power Electron.* **2018**, *33*, 2447–2457. [CrossRef]

15. Huang, Y.; Yang, K.; Luo, C.; Li, R.; Luo, Y. Sensorless Model Predictive Current Control for SynRM Based on Alternate High-Frequency Square-wave Voltage Injection. In Proceedings of the 2023 IEEE International Conference on Predictive Control of Electrical Drives and Power Electronics (PRECEDE), Wuhan, China, 16–19 June 2023.

16. Yu, K.; Wang, Z. Online Decoupled Multi-parameter Identification of Dual Three-Phase IPMSM Under Position-Offset and HF Signal Injection. *IEEE Trans. Ind. Electron.* **2023**, *71*, 3429–3440. [CrossRef]

17. Lee, H.J.; Joo, J.E.; Lee, H.J.; Yoon, Y.D. A Torque Reference Limiter to Avoid Unstable Region of High-Frequency Signal Injection-Based Sensorless Control. In Proceedings of the 2022 IEEE Transportation Electrification Conference & Expo (ITEC), Anaheim, CA, USA, 15–17 June 2022; pp. 692–696.

18. Wang, G.; Xiao, D.; Zhao, N.; Zhang, X.; Wang, W.; Xu, D. Low-Frequency Pulse Voltage Injection Scheme-Based Sensorless Control of IPMSM Drives for Audible Noise Reduction. *IEEE Trans. Ind. Electron.* **2017**, *64*, 8415–8426. [CrossRef]

19. Tang, Q.P.; Shen, A.; Luo, X.; Xu, J. IPMSM Sensorless Control by Injecting Bi-directional Rotating HF Carrier Signals. *IEEE Trans. Power Electron.* **2018**, *33*, 10698–10707. [CrossRef]

20. Lara, J.; Chandra, A. Performance Investigation of Two Novel HSFSI Demodulation Algorithms for Encoderless FOC of PMSMs Intended for EV Propulsion. *IEEE Trans. Ind. Electron.* **2018**, *65*, 1074–1083. [CrossRef]

21. Almarhoon, A.H.; Zhu, Z.Q.; Xu, P. Improved Rotor Position Estimation Accuracy by Rotating Carrier Signal Injection Utilizing Zero-Sequence Carrier Voltage for Dual Three-Phase PMSM. *IEEE Trans. Ind. Electron.* **2017**, *64*, 4454–4462. [CrossRef]

22. Weber, B.; Wiedmann, K.; Mertens, A. Increased signal-to-noise ratio of sensorless control using current oversampling. In Proceedings of the 2015 9th International Conference on Power Electronics and ECCE Asia (ICPE-ECCE Asia), Seoul, Republic of Korea, 1–5 June 2015.

23. Medjmadj, S.; Diallo, D.; Mostefai, M.; Delpha, C.; Arias, A. PMSM Drive Position Estimation: Contribution to the High-Frequency Injection Voltage Selection Issue. *IEEE Trans. Energy Convers.* **2015**, *30*, 349–358. [CrossRef]
24. Wang, G.; Yang, L.; Zhang, G.; Zhang, X.; Xu, D. Comparative Investigation of Pseudorandom High-Frequency Signal Injection Schemes for Sensorless IPMSM drives. *IEEE Trans. Power Electron.* **2017**, *32*, 2123–2132. [CrossRef]
25. Stumberger, G.; Dolinar, D.; Hamler, A. Cross Magnetization Effect on Inductances of Linear Synchronous Reluctance Motor Under Load Conditions. *IEEE Trans. Magn.* **2001**, *37*, 3658–3662. [CrossRef]
26. Im, J.-B.; Kim, W.; Kim, K.; Jin, C.-S.; Choi, J.-H.; Lee, J. Inductance Calculation Method of Synchronous Reluctance Motor Including Iron Loss and Cross Magnetic Saturation. *IEEE Trans. Magn.* **2009**, *45*, 2803–2806.
27. Liu, J.M.; Zhu, Z.Q. Novel sensorless control strategy with injection of high-frequency pulsating carrier signal into stationary reference frame. *IEEE Trans. Ind. Appl.* **2014**, *50*, 2574–2583. [CrossRef]
28. Wang, M.; Sun, D.; Ke, W.; Nian, H. A Universal Lookup Table-Based Direct Torque Control for OW-PMSM Drives. *IEEE Trans. Power Electron.* **2021**, *36*, 6188–6191. [CrossRef]
29. Jang, J.-H.; Sul, S.-K.; Ha, J.-I.; Ide, K.; Sawamura, M. Sensorless Drive of Surface-Mounted Permanent-Magnet Motor by High-Frequency Signal Injection Based on Magnetic Saliency. *IEEE Trans. Ind. Appl.* **2003**, *39*, 1031–1039. [CrossRef]
30. Bi, G.; Wang, G.; Zhang, G.; Xu, D. A Novel Demodulation Method Based High-Frequency Signal Injection for Sensorless SPMSM Control Considering Cross-Saturation Effect. In Proceedings of the 2018 IEEE 27th International Symposium on Industrial Electronics (ISIE), Cairns, Australia, 12–15 June 2018; pp. 95–100.
31. Sujitha, A.; Lakshmi, L.; Mathan, N.; Narmadha, R. Analysis of an Efficient Linear Congruential Generator Architecture for Digital Applications. In Proceedings of the 2023 Fifth International Conference on Electrical, Computer and Communication Technologies (ICECCT), Erode, India, 22–24 February 2023; pp. 1–4.
32. Li, C.; Wang, G.; Zhang, G.; Xu, D.; Xiao, D. Saliency-Based Sensorless Control for SynRM Drives with Suppression of Position Estimation Error. *IEEE Trans. Ind. Electron.* **2019**, *66*, 5839–5849. [CrossRef]